Discrete dislocation modeling of fatigue crack propagation

V.S. Deshpande [a], A. Needleman [a,*], E. Van der Giessen [b]

[a] *Division of Engineering, Brown University, Providence, RI 02912-9104, USA*
[b] *Department of Applied Physics, University of Groningen, Nyenborgh 4, 9747 AG Groningen, The Netherlands*

Abstract

Analyses of the growth of a plane strain crack subject to remote mode I cyclic loading under small-scale yielding are carried out using discrete dislocation dynamics. Cracks along a metal–rigid substrate interface and in a single crystal are studied. The formulation is the same as that used to analyze crack growth under monotonic loading conditions, differing only in the remote stress intensity factor being a cyclic function of time. Plastic deformation is modeled through the motion of edge dislocations in an elastic solid with the lattice resistance to dislocation motion, dislocation nucleation, dislocation interaction with obstacles and dislocation annihilation being incorporated through a set of constitutive rules. An irreversible relation is specified between the opening traction and the displacement jump across a cohesive surface ahead of the initial crack tip in order to simulate cyclic loading in an oxidizing environment. The cyclic crack growth rate $\log(\mathrm{d}a/\mathrm{d}N)$ versus applied stress intensity factor range $\log(\Delta K_I)$ curve that emerges naturally from the solution of the boundary value problem shows distinct threshold and Paris law regimes. Paris law exponents in the range 4 to 8 are obtained for the parameters employed here. Furthermore, rather uniformly spaced slip bands corresponding to surface striations develop in the wakes of the propagating cracks. © 2002 Acta Materialia Inc. Published by Elsevier Science Ltd. All rights reserved.

1. Introduction

For fatigue crack growth in a wide variety of engineering materials under remote mode I loading, there is a threshold value of $\Delta K_I = K_{\max} - K_{\min}$ below which cracks do not grow at a detectable rate. Above this threshold value, in the regime where the amount of crack growth per cycle,

da/dN, is of the order of a few lattice spacings, there is a steep increase in $\mathrm{d}a/\mathrm{d}N$ with ΔK_I. For larger values of ΔK_I, the increase in $\mathrm{d}a/\mathrm{d}N$ becomes less steep and the Paris law regime (Paris et al. [1]) is entered where $\mathrm{d}a/\mathrm{d}N \propto (\Delta K_I)^m$. A critical review of work on fatigue crack growth mechanisms from the threshold through the Paris law regimes is given by Davidson and Lankford [2].

There are a number of characteristic features of the crack growth behavior in the Paris regime [2]. Experimentally, the value of the Paris exponent m ranges widely; values of 2–4 are typically reported for ductile metals, e.g. [3,4], while values varying

---

* Corresponding author. Tel.: +1-401-863-2863; fax: +1-401-863-1157.

E-mail address: needle@engin.brown.edu (A. Needleman).

from 4.5 to as high as 40 have been seen for inter-metallics and nickel-based superalloy single crys-tals [5,6]. Slip striations are commonly observed with a spacing that is of the order of the amount of crack growth per cycle. In contrast, when stri-ations are observed in the threshold regime, their spacing is generally much greater than the amount of crack growth per cycle. In some cases, steady cycle-by-cycle crack growth rates have been observed, while in other cases crack growth is reported to be intermittent [7] so that a steady growth rate is only apparent, arising from averag-ing the growth rate over many cycles.

Many continuum theories have been proposed to rationalize the dependence of the fatigue crack growth rate on ΔK_I in the Paris regime. The geo-metrical models, by for example Laird and Smith [8] and McClintock [9], presume that the crack growth rate is proportional to the cyclic crack opening displacement which, in turn, is pro-portional to $(\Delta K_I)^2$. Hence, geometrical models predict a Paris exponent $m = 2$. Damage accumu-lation models, such as those of McClintock [10], Weertman [11] and Rice [12], give rise to a Paris exponent $m = 4$. McClintock [10] used a critical strain-based failure criterion while Rice [12] used a critical value of the absorbed hysteresis energy. More recently, Nguyen et al. [13] reported numeri-cal calculations of fatigue crack growth in which the material was characterized by a conventional continuum plasticity model and the fracture properties were embedded in a cohesive relation. Non-dissipative cohesive relations resulted in plas-tic shakedown after a few cycles with no further crack growth. Thus, Nguyen et al. [13] employed a cohesive law with loading–reloading hysteresis and obtained Paris-like behavior with $m \approx 3$. None of the above continuum models account for the wide range of Paris exponents observed exper-imentally. Furthermore, these models are restricted to the Paris law regime and do not predict the change in the dependence on ΔK_I that occurs near the fatigue threshold.

Recent literature on dislocation models for fatigue crack growth has been reviewed by Rie-melmoser et al. [14]. These dislocation models, by for example Pippan and co-workers [15–17] and Wilkinson et al. [18], are meant to represent the deformation-controlled fatigue crack growth mech-anism proposed by Laird and Smith [8] and Neum-ann [19]. In particular, Neumann's model is based on a mechanism that accounts for crack growth as well as striations by an alternating duplex slip mechanism. It is worth noting that striation forma-tion is observed in fatigue crack growth at metal–ceramic interfaces [20–22] even though the kin-ematics of crack growth by an alternating slip mechanism is not clear for a crack growing along such an interface.

Here, we analyze the transition from near-thres-hold to Paris law behavior using a unified frame-work that is applicable in both the near-threshold and Paris law regimes. Indeed, a key feature of our approach is that the material model and the fracture properties are independent of whether the loading is monotonic or cyclic. In fact, the material model is applicable whether or not there is a crack, see e.g. [23]. The fracture properties are embedded in a cohesive surface constitutive relation. As a consequence, crack initiation and crack growth emerge as natural outcomes of the boundary value problem solution. In contrast to the solely defor-mation-controlled crack growth mechanism assumed in [15–18], crack growth in our calcu-lations is stress as well as deformation driven. The normal separation of the newly formed crack sur-faces, which gives rise to an open crack, occurs without requiring a particular crack tip slip mode.

As in our previous study [24] of near-threshold fatigue crack growth, a plane strain small-scale yielding boundary value problem is formulated and solved in the small-strain limit. The deforming material is a planar model crystal with three slip systems. Plastic flow arises from the collective motion of large numbers of edge dislocations, which are represented as line singularities in an elastic solid. Drag during dislocation motion, inter-actions with obstacles, and dislocation nucleation and annihilation are accounted for. The irreversi-bility of dislocation motion is what gives rise to continued crack growth under cyclic loading [24].

Most calculations are carried out for a ductile metal single crystal bonded to a rigid substrate, representing a metal–ceramic interface. In addition, for comparison purposes, some calculations are carried out for a crack in a homogeneous metal

single crystal. Considering a metal–ceramic interface has several advantages over the homogeneous material case: (i) crack growth along interfaces occurs when the interfacial cohesive strength is lower than that of the surrounding homogeneous materials; with decreasing cohesive strength the plastic zone size decreases, which reduces the computational time and decreasing cohesive strength increases the effective cohesive length, which improves numerical accuracy for a given mesh resolution [25]; (ii) along a bimaterial interface, crack growth often occurs along the interface so that our assumption of straight-ahead crack growth is appropriate; and (iii) even though straight-ahead crack growth occurs, the mismatch in material properties allows mixed-mode loading effects to be explored. In addition, fatigue crack growth along metal–ceramic interfaces is of interest in its own right, see [20–22,26].

2. Discrete dislocation formulation

Details of the boundary value problem to be solved are illustrated in Fig. 1. As mentioned above, most calculations are for a crack along the interface between a single crystal and a rigid substrate. The analyses are two dimensional, under plane strain, and the crystal is taken to have three slip systems, to mimic the ambiguity of slip that exists in three-dimensional FCC crystals. Two slip systems have their slip planes oriented at $\theta = \pm 60°$ from the interface, the third one at $\theta = 0°$.[1] Assuming small-scale yielding, plastic deformation near the crack tip by the motion of discrete dislocations is accounted for in a process window of dimensions $L_p = 15$ μm by $h_p = 15$ μm. The size of the rectangular region analyzed is 1000 μm×500 μm.

The dislocations are treated as singularities in an elastic continuum, where for computational convenience, the crystal is assumed to be elastically
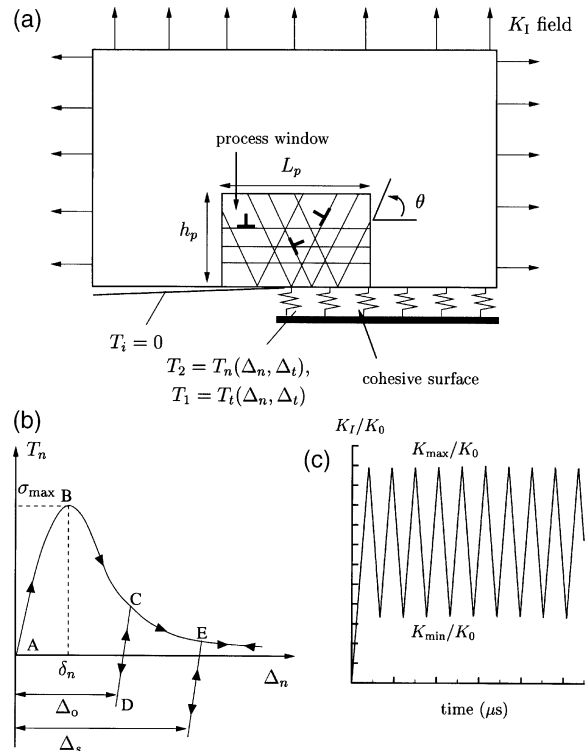

Fig. 1. (a) Interface crack problem with the imposed boundary conditions. (b) Irreversible cohesive law. (c) Schematic of the applied stress intensity factor as a function of time.

isotropic with shear modulus $\mu = 26.3$ GPa and Poisson's ratio $\nu = 0.33$, which are representative values for aluminum. Consistent with the plane strain condition, only edge dislocations are considered, all having the same Burgers vector, $b = 0.25$ nm. The potentially active slip planes in the process window are spaced at $100b$. As suggested by Kubin et al. [27], the following dislocation mechanisms are incorporated: (i) dislocation glide; (ii) annihilation; (iii) nucleation; (iv) obstacle pinning. The glide velocity is taken to be linearly related to the Peach–Koehler force with a drag coefficient $B = 10^{-4}$ Pa s, a representative value for several FCC crystals. Dislocations of opposite sign annihilate when they come within a critical distance of $L_e = 6b$. Initially, the three slip systems are supposed to be dislocation free, but dislocations can be generated from discrete sources that are randomly distributed in the process window with a density of 66/μm². These point sources

---

[1] In our previous study [24] we analyzed a crystal with two slip systems at $\theta = \pm 60°$ and found that the qualitative features of near-threshold fatigue were similar to those of the FCC-like crystal with three slip systems.

mimic Frank–Read sources from pinned segments on out-of-plane slip systems which are not explicitly considered. They generate a dipole when the Peach–Koehler force exceeds a critical value of $\tau_{nuc}b$ during a period of time τ_{nuc}; here $\tau_{nuc} =$ 50 MPa and $t_{nuc} = 10$ ns. There is no special dislocation nucleation from the crack tip. The process window also contains a random distribution of 170 point obstacles per μm^2, which can represent either small precipitates on the slip plane or forest dislocations on out-of-plane slip systems. The obstacles pin dislocations as long as the Peach–Koehler force is below the obstacle strength $b\tau_{obs}$, where $\tau_{obs} =$ 150 MPa.

Ahead of the crack, a cohesive surface is assumed, with properties specified by relations between the normal (T_n) and tangential (T_t) tractions across this surface and the corresponding displacement jumps (Δ_n, Δ_t). These relations, which include the mixed-mode failure properties of the interface between the single crystal and the substrate, are derived from a potential ϕ [28] as

$$T_i = -\frac{\partial\phi}{\partial\Delta_i}, \ (i = n,t) \tag{1}$$

with

$$\phi = \phi_n + \phi_n \exp\left(-\frac{\Delta_n}{\delta_n}\right)\left\{\left[1-r+\frac{\Delta_n}{\delta_n}\right]\right. \tag{2}$$
$$\frac{1-q}{r-1}-\left[q+\left(\frac{r-q}{r-1}\right)\frac{\Delta_n}{\delta_n}\right]\exp\left(-\frac{\Delta_t^2}{\delta_t^2}\right)\left.\right\}.$$

The normal work of separation, ϕ_n, and the shear work of separation, ϕ_t, can be expressed as

$$\phi_n = e\sigma_{max}\delta_n, \ \phi_t = \sqrt{\frac{e}{2}}\tau_{max}\delta_t \tag{3}$$

in terms of the normal strength σ_{max} and tangential strength τ_{max}, and the characteristic lengths δ_n and δ_t ($e = \exp(1)$). The coupling between normal and tangential separation is governed by $q = \phi_t / \phi_n$ and $r = \Delta_n^* / \delta_n$, where Δ_n^* is the value of Δ_n after complete shear separation with $T_n = 0$. The cohesive surface characteristic lengths are taken to be $\delta_n = \delta_t = 0.5$ nm for the interface. Also, the ratio of τ_{max} to σ_{max} is fixed at 2.33 so that $\phi_n = \phi_t$ and we take $r = 0$. The cohesive strengths are taken as $\sigma_{max} = 0.3$ GPa and $\tau_{max} = 0.699$ GPa and thus

$\phi_n = \phi_t = 0.408$ J m^{-2}. Such strengths are consistent with experimental measurements of intrinsic metal–ceramic interface strengths in [29]. The work of separation is related to a reference stress intensity factor K_0 by the small-scale yielding relation

$$K_0 = \sqrt{\frac{E\phi_n}{1-v^2}}. \tag{4}$$

The significance of K_0 is that pure mode I crack growth in a homogeneous elastic solid with the given cohesive properties takes place at $K_I / K_0 = 1$ [30]. For the material parameters used in this interface problem $K_0 = 0.179$ MPa $\sqrt{m}$. Note that the quantity K_0 is a measure of the energy per unit area required to create new free surface. The fracture strength under monotonic loading conditions, K_{Ic}, will in general be significantly greater than K_0 due to plastic dissipation.

The cohesive law described above gives rise to reversible behavior of the interface and can be used under monotonic loading and under cyclic loading in a non-oxidizing environment (vacuum). In oxidizing environments, oxidation of the new surfaces formed by crack growth inhibits crack closure and hence the cohesive law needs to be irreversible. Our implementation of this is illustrated by the T_n–Δ_n response in Fig. 1b. The relations (1)–(3) describe the loading response as the traction increases from A up to the maximum value at B, followed by softening while the formed crack opens further. Unloading from any point C now is specified to take place along path CD, with the stiffness against normal separation given by

$$\frac{\partial T_n}{\partial\Delta_n} = -\frac{e\sigma_{max}}{\delta_n}. \tag{5}$$

Upon reloading the traction increases along DC and then follows the original softening curve BCE. All other stiffnesses are unchanged from the reversible cohesive relation (i.e. derived from the potential ϕ). Thus, the irreversible cohesive relation accounts for premature surface contact due to oxide formation but neglects any irreversibility in the tangential tractions. As the normal opening gradually increases with continued cyclic loading, the permanent opening Δ_o grows, but not more

than a predefined value of Δ_s. This represents the asymptotic value of the oxide layer thickness formed on a metal surface: under ambient conditions this is reported to be between 2 and 6 nm for aluminum [31] and in the calculations we take $\Delta_s = 4$ nm.

Apart from the traction-free crack and the cohesive surface ahead of the crack, the boundaries of the region analyzed are subjected to displacement boundary conditions corresponding to a mode I isotropic linear elastic crack tip field. Analytical expressions are available for two limiting cases. For a crack along a perfectly bonded interface, the near-tip fields are inherently mixed mode involving both mode I (tension) and mode II (shear), even for remote tensile loading, with the mode I to mode II ratio varying with distance from the crack tip, e.g. [32,33]. The variation with distance from the crack tip is oscillatory, with the oscillatory index depending on the elastic mismatch, and involves an arbitrary reference length. On the other hand, if the shear cohesive stiffness of the interface is zero, the much simpler homogeneous mode I linear elastic crack tip fields (e.g. [3], Chapter 14) prevail. Neither of these is an exact solution for the relatively weak interfaces considered. In the calculations here, displacement boundary conditions having the form of the homogeneous mode I linear elastic crack tip field are imposed. This has the advantage, for the rectangular region analyzed, of avoiding having to specify an arbitrary reference length. Even though the homogeneous mode I field is prescribed on the remote boundary, the stiffness mismatch between the crystal and the substrate gives rise to mixed-mode loading conditions within the region analyzed.

The applied stress intensity factor, K_I, is prescribed to cycle between a maximum value of K_{max} and a minimum value K_{min} as shown in Fig. 1c. The loading frequency is chosen such that the loading rate $|\dot{K}_I|$ has a constant value of 100 GPa $\sqrt{m}$/s (this high value is chosen for computational reasons and is not expected to affect the results qualitatively [34]). The duration of a cycle is $2\Delta K_I / |\dot{K}_I|$, and with the interface properties mentioned above, can be expressed as $3.6 \, \Delta K_I/K_0$ µs.

The boundary value problem thus defined is nonlinear and is solved in an incremental manner

as discussed in detail in [24,35]. For each time step, the long-range fields of the dislocations and the resulting Peach–Koehler forces between them are determined by means of a superposition method [36]. The central idea is to decompose these fields into the analytical singular fields of individual dislocations in a half-space, and image fields to correct for the boundary conditions. The latter are nonsingular and are obtained with a finite element method (using a graded mesh of 90 by 90 elements in the process window). The singular part of the fields and the discontinuities in the displacement fields are represented analytically.

Some computations are carried out for a crack in a metal single crystal, as in our previous study of the near-threshold regime [24]. The problem sketched in Fig. 1a is then the symmetric half of the total problem with $\Delta_t = T_t = 0$. The material parameters are as specified previously while the cohesive surface properties are taken to be $\sigma_{max} = 0.5$ GPa, $\delta_n = 0.75$ nm and $\Delta_s = 6$ nm giving $K_0 = 0.283$ MPa $\sqrt{m}$ ($\phi_n = 1.02$ J m^{-2}). This value of σ_{max} is about a factor of four smaller than is representative of the theoretical strength of aluminum. We employ this small value of σ_{max} so as to decrease the plastic zone size and increase the cohesive length in order to reduce the computation time and increase accuracy. Note that here Δ_n is the total normal separation of the cohesive surface, $\Delta_n = 2u_2(x_1,0)$, where $x_2 = 0$ gives the crack plane.

3. Numerical results

In the calculations presented here the applied stress intensity factor K_I was varied between K_{min} and K_{max} as shown in Fig. 1c. The ratio $R = K_{min} / K_{max}$ and the difference $\Delta K_I = K_{max} - K_{min}$ are used to characterize the cyclic loading. Simulations were carried out with a fixed R and the applied ΔK_I varied to get cycle-by-cycle crack growth rates da/dN typically in the range 5×10^{-4} to 0.1 µm/cycle.

3.1. Fatigue at an interface

We present cyclic loading results for three values of the load ratio, R, 0.1, 0.3 and 0.5. First

the case with $R = 0.3$ is considered. Crack advance (Δa) versus time curves for a threshold, intermediate and high value of applied ΔK_{I} are shown in Fig. 2a. Here and subsequently the crack tip location is taken to be the point along the cohesive surface where $\Delta_n = 4\delta_{\mathrm{n}}$.[2] In the three cases shown $K_{\max}$ is higher than required for crack growth to initiate under monotonic loading conditions so a "burst" of crack growth occurs during the first loading cycle. Subsequently, the incremen-

tal cycle-by-cycle crack growth behavior is qualitatively different in the three cases shown in Fig. 2a. Approximately equal amounts of crack advance per cycle corresponding to "steady" cycle-by-cycle crack growth rates $\mathrm{d}a / \mathrm{d}N \approx 5 \times 10^{-4}$ and 0.03 μm/cycle occur for $\Delta K_{\mathrm{I}} / K_0 = 0.756$ and 1.05, respectively. On the other hand, crack growth is more intermittent at the intermediate value of $\Delta K_{\mathrm{I}} / K_0 = 0.938$. At this intermediate ΔK_{I} value, small amounts of cycle-by-cycle crack growth are intermingled with occasional spurts of relatively large crack advance resulting in an average $\mathrm{d}a / \mathrm{d}N \approx 0.02$ μm/cycle over the 36 cycles computed. No measurable cycle-by-cycle crack growth was obtained with $\Delta K_{\mathrm{I}} / K_0 < 0.756$.

The evolution of the dislocation density ρ_{dis} (per unit area in the process window) with time is shown in Fig. 2b for the cases discussed above. For $\Delta K_{\mathrm{I}} / K_0 = 0.938$ and 1.05 there is a clear increase in the dislocation density with number of loading cycles. Consequently, the dislocation structures at the end and at the beginning of each cycle differ. This is illustrated in Figs 3a and b which show the dislocation structures around the crack tip after the third and twelfth load peaks, respectively for the case with $\Delta K_{\mathrm{I}} / K_0 = 1.05$. The irreversibility of dislocation motion results in an evolving dislocation structure with cyclic loading so that the crack can grow to different lengths during different loading cycles. On the other hand, the very low crack growth rate with $\Delta K_{\mathrm{I}} / K_0 = 0.756$ results in nearly no cycle-by-cycle change in dislocation density indicating that this loading state is near the plastic shakedown limit. This is consistent with the fact that no cyclic crack advance is observed for $\Delta K_{\mathrm{I}} / K_0 < 0.756$.

Experimentally, slip traces in the wake of the propagating fatigue crack are usually observed in optical micrographs and are cited as evidence for the alternating slip mechanism of fatigue crack propagation, e.g. [8,19]. While the kinematics of crack growth along an interface by a duplex slip-type mechanism is unclear, fatigue striations on the fracture surface and discrete slip traces on the metal surface in the wake of the propagating crack are also seen in cyclic crack growth at interfaces [20–22]. In order to compare the predictions of the
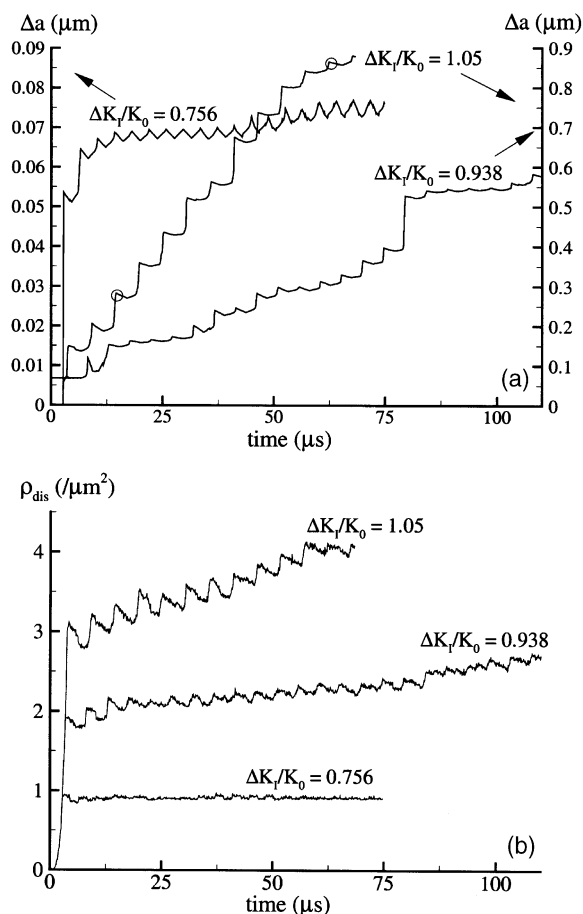

Fig. 2. (a) Time evolution of the crack growth and (b) time evolution of the dislocation density for the interface crack ($R = 0.3$).

---

[2] In all the calculations presented here, the crack advance (Δa) identified by a specified amount of normal separation always exceeded the crack advance based on that amount of tangential separation.
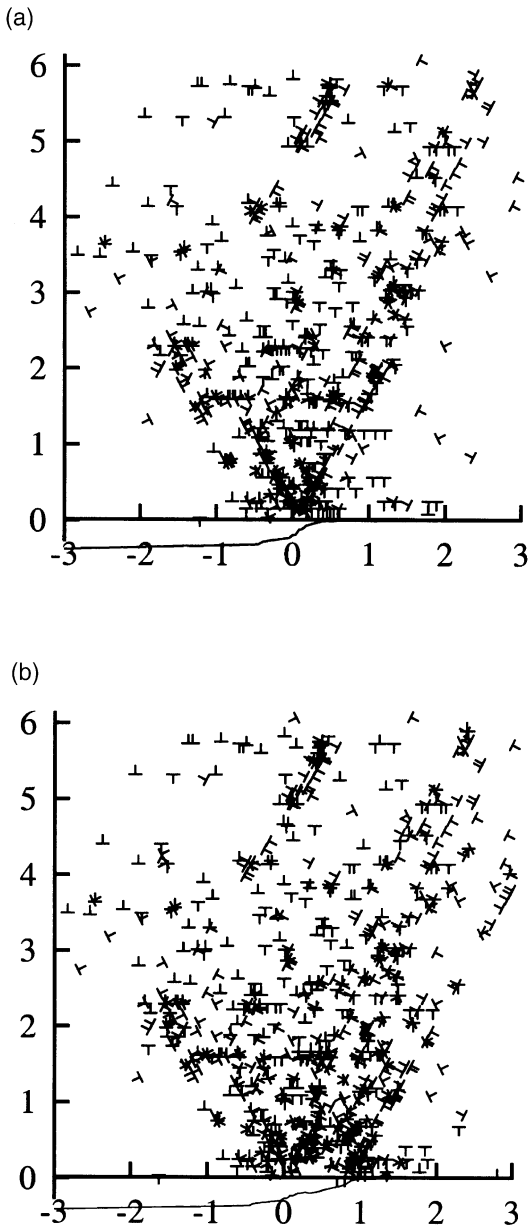
(a)

(b)

Fig. 3. Dislocation structures for interface crack ($R = 0.3$, $\Delta K_{\mathrm{I}} / K_0 = 1.05$) at (a) the 3rd and (b) the 12th load peak as marked in Fig. 2a. All distances are in μm. The crack opening profiles (displacements magnified by a factor of 20) are plotted below the x_1-axis.

discrete dislocation simulations with these experimental observations, the deformation pattern predicted by the discrete dislocation calculation is illustrated by plotting slip contours. The calculated displacement field is not continuous; dislocation glide gives rise to a displacement jump across the slip plane. However, to visualize the deformations, the values of the displacements u_i are evaluated on a uniform rectangular grid with spacing 0.02 μm (this grid is finer than the finite element grid). The strain field ϵ_{ij} given by

$$\epsilon_{ij} = \frac{1}{2}\left(\frac{\partial u_i}{\partial x_j} + \frac{\partial u_j}{\partial x_i}\right) \tag{6}$$

is then obtained by numerical differentiation. The slip $\gamma^{(\alpha)}$ is defined by[3]

$$\gamma^{(\alpha)} = s_i^{(\alpha)}\epsilon_{ij}m_j^{(\alpha)} \tag{7}$$

where $s_i^{(\alpha)}$ is the tangent and $m_j^{(\alpha)}$ is the normal to slip plane α.

The total slip over the three slip systems, $\Gamma = \sum_{\alpha = 1}^{3} |\gamma^{(\alpha)}|$ is shown at the third and twelfth load peaks in Figs 4a and b, respectively, for a loading characterized by $R = 0.3$ and $\Delta K_{\mathrm{I}} / K_0 = 1.05$. At the third load peak, contours of Γ in Fig. 4a show strong evidence of slip traces emanating from the original crack tip on the $\theta = \pm 60°$ slip planes. By the twelfth load peak (Fig. 4b) discrete slip traces have formed at intervals of ≈ 0.15 μm on the $\theta = 60°$ planes in the wake of the propagating crack. These are very similar to those seen in the experimental investigations of [20,22] for cyclic crack advance at Al–Al$_2$O$_3$ interfaces.

The cyclic crack growth rate da/dN in the duplex slip model scales with the slip band spacing. Experimental observations of cyclic crack growth at interfaces [20] and in single crystals [2], however, indicate that this spacing is generally larger than da/dN and this difference increases with decreasing ΔK_{I}. In Fig. 4c contours of Γ at the 36th load peak are shown for $\Delta K_{\mathrm{I}} / K_0 = 0.938$ ($R =$

---

[3] The quantity $\gamma^{(\alpha)}$ is not the actual slip on slip plane α as it includes contributions from dislocations gliding on all slip systems. However, it is a convenient quantity for picturing the deformation pattern.
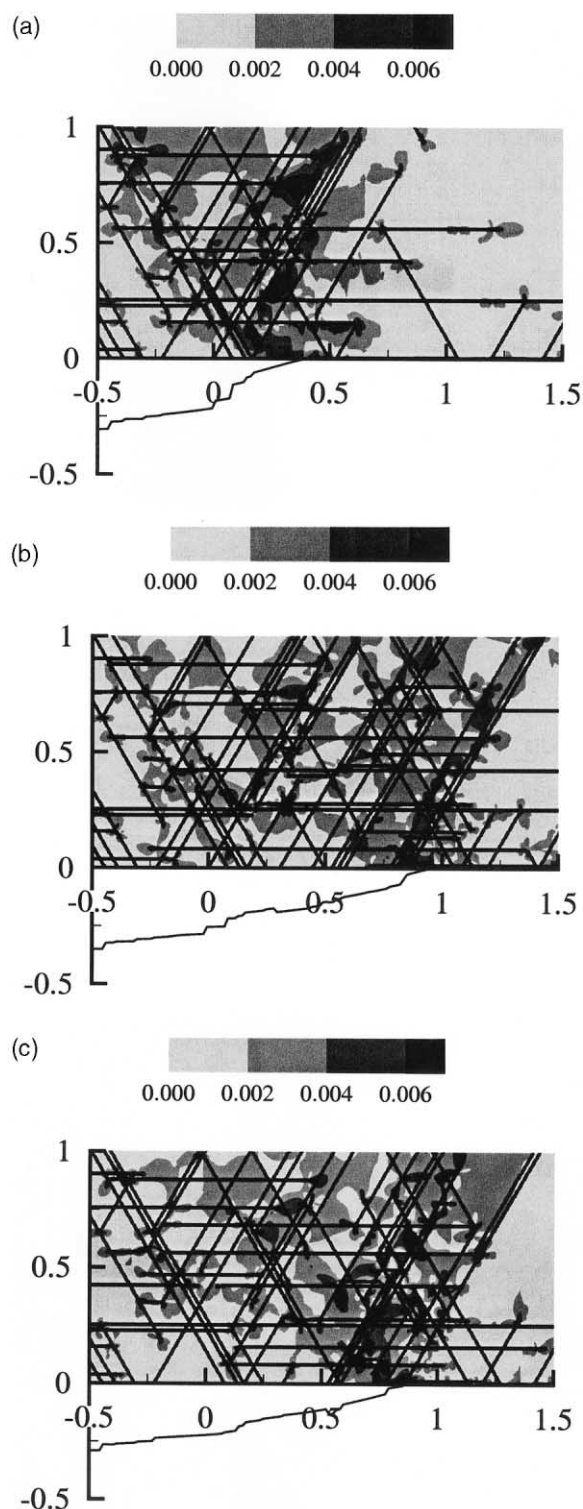
0.3): the crack advance in this case of $\Delta a \approx 0.8$ μm is approximately equal to that after 12 cycles with $\Delta K_{\mathrm{I}} / K_0 = 1.05$. The slip band spacing in Fig. 4c is less uniform with an average value ≈ 0.2 μm. Consistent with experimental observations, the slip band spacing in both Figs 4b and c is greater than the respective values of da/dN, with the ratio of slip band spacing to the average da/dN being approximately 2.7 and 8.6 for $\Delta K_{\mathrm{I}} / K_0 = 1.05$ and 0.938, respectively.

For comparison purposes, a calculation was carried out with K_{I} monotonically increasing. The curve of K_{I} versus crack advance Δa is shown in Fig. 5a. Here, as seen by Cleveringa et al. [35], crack growth occurs in "spurts." Contours of Γ at the instant marked in Fig. 5a are shown in Fig. 5b. This corresponds to a crack advance $\Delta a \approx 0.8$ μm which is approximately equal to that achieved after 12 and 36 cycles for the cases plotted in Figs 4b and c, respectively. Similar to the slip traces in Fig. 4, slip bands at discrete intervals also occur in Fig. 5b. The major difference here is that the higher applied K_{I} required to propagate the crack by 0.8 μm under monotonic loading results in an increase in the distributed plasticity. The slip bands, which tend to arrest the crack intermittently, are consistent with the sporadic nature of the monotonic fracture process [35]. Thus, even though the same crack growth mechanism operates under both monotonic and cyclic loadings, continued crack growth occurs under cyclic loading at a value of K_{max} for which the crack would have arrested under monotonic loading: the different dislocation structures at the beginning and end of each loading cycle permit progressive cyclic crack growth. To illustrate this point K_{max}/K_0 versus the crack extension Δa is shown for two cyclic loading cases along with the monotonic K_{I}/K_0 versus crack advance curve in Fig. 5a. While the $\Delta K_{\mathrm{I}} / K_0 = 0.938$ ($R = 0.3$) calculation was carried out for 36 cycles resulting in a crack extension of ≈ 0.8 μm, the $\Delta K_{\mathrm{I}} / K_0 =$

Fig. 4. Contours of the total slip $\Gamma = \sum |\gamma^{(\alpha)}|$ at (a) the 3rd and (b) the 12th load peak for $R = 0.3$ and $\Delta K_{\mathrm{I}} / K_0 = 1.05$ as marked in Fig. 2a, and (c) at the 36th load peak for $R = 0.3$ and $\Delta K_{\mathrm{I}} / K_0 = 0.938$. All distances are in μm. The crack opening profiles (displacements magnified by a factor of 20) are plotted below the x_1-axis.
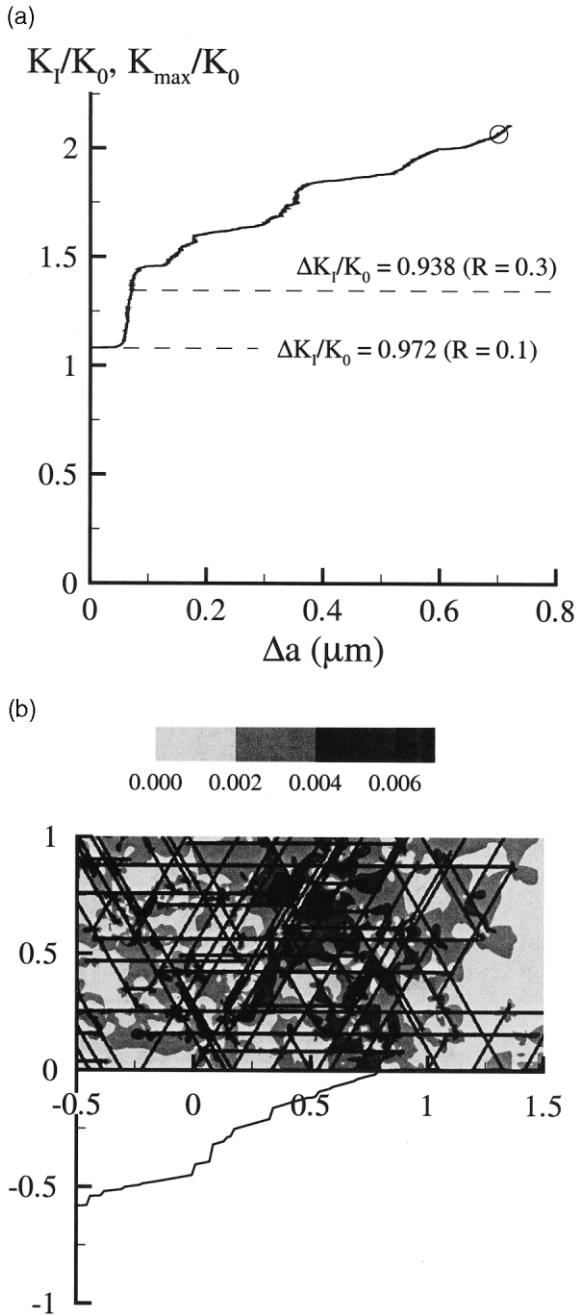
(a)

K_I/K_0, K_{max}/K_0

$\Delta K_I/K_0 = 0.938$ (R = 0.3)

$\Delta K_I/K_0 = 0.972$ (R = 0.1)

Δa (μm)

(b)

0.000   0.002   0.004   0.006

Fig. 5.   (a) The applied stress intensity factor K_I/K_0 as a function of the crack extension Δa for monotonic loading of the interface crack. (b) Contours of the total slip $\Gamma = \sum |\gamma^{(\alpha)}|$ at the point marked in Panel a. All distances are in μm. The crack opening profile (displacements magnified by a factor of 20) is plotted below the x_1-axis.

0.972 ($R = 0.1$) calculation was carried out for 20 cycles resulting in $\Delta a \approx 0.27$ μm. In both cases, continued crack growth occurs under cyclic loading at a value of K_{max} for which the crack would have arrested under monotonic loading.

Cyclic loading calculations similar to those described above were carried out for various values of R and ΔK_I. The results of those calculations are summarized in Fig. 6a where we plot da/dN versus the applied ΔK_I. The da/dN values plotted are averages over the number of cycles computed in each case. This was typically 20 cycles in the low ΔK_I

(a)

da/dN (μm/cycle)

da/dN v. ΔK_I^{eff}

4.13   6.48   1

1   8.55   1   6.33

ΔK_{th}

ΔK_{th}^{eff} ΔK_{th} ΔK_{th}

R = 0.1
R = 0.3
R = 0.5

$\Delta K_I/K_0$, $\Delta K_I^{eff}/K_0$

(b)

K_{op}/K_{max}

R = 0.1
R = 0.3
R = 0.5

$\Delta K_I/K_0$
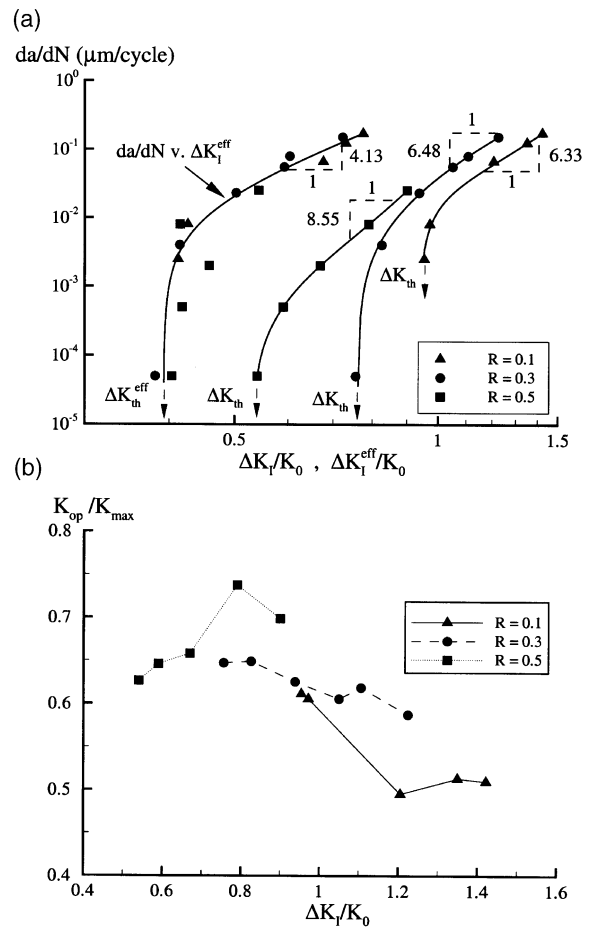
Fig. 6.   (a) The cyclic crack growth rate da/dN versus $\Delta K_I/K_0$ and $\Delta K_I^{eff}/K_0$ for the mode I cyclic loading of the interface crack. The slopes of the curves marked correspond to the Paris law exponents for the curves fitted through the numerical results. (b) The normalized crack-opening stress intensity factor K_{op}/K_{max} versus $\Delta K_I/K_0$.

regime and at least 10 cycles in the high ΔK_I regime. Use of other definitions of da/dN was explored, e.g. maximum or minimum crack growth in any cycle computed; while such definitions changed the numerical values of the da/dN versus ΔK_I relation, no change in the qualitative response was seen.

The $\log(da/dN)$ versus $\log(\Delta K_I/K_0)$ curves in Fig. 6a show two distinct stages of fatigue crack growth behavior. In the first regime, the average crack growth per cycle is smaller than a lattice spacing with the crack either remaining dormant or growing at undetectable rates below a threshold value ΔK_{th}. Just above the threshold, da/dN increases sharply with ΔK_I. Subsequently, there is a "knee" in the $\log(da/dN)$ versus $\log(\Delta K_I/K_0)$ curve with da/dN increasing more gradually with increasing ΔK_I. This regime, which is referred to as the Paris law regime, is characterized by a power law relation between da/dN and ΔK_I,

$$\frac{da}{dN} \propto \Delta K_I^m. \tag{8}$$

For the simulations presented here we see from Fig. 6a that the Paris law exponent m lies between approximately 6 and 8 depending on the value of R. As in [24], the fatigue threshold ΔK_{th} decreases with increasing R. However, with increasing ΔK_I the dependence of the crack growth rates on R diminishes and the $\log(da/dN)$ versus $\log(\Delta K_I/K_0)$ curves for the three R values in Fig. 6a are tending to converge.

In our previous study [24] we found that the fatigue threshold with an irreversible cohesive law occurs at a constant effective threshold stress intensity factor range ΔK_{th}^{eff} with the dependence of the crack growth rates on R a result of crack closure. When the crack faces are in contact, the stresses in the vicinity of the crack tip are much reduced, inhibiting dislocation nucleation and glide as well as lowering the driving force for separation. As a consequence, crack propagation tends to take place only during the fraction of the fatigue loading cycle in which the crack faces are separated, see for example [37,38]. We thus proceed to quantify the effect of crack closure and investigate the origin of the dependence of da/dN on R in the post-threshold as well in the threshold regime.

The unloading path specified for the normal tractions in the irreversible cohesive law simulates surface contact due to the formation of oxide layers on the newly formed surfaces; locations along the cohesive surface where the opening Δ_n exceeds $4\delta_n$ but are under the action of compressive surface tractions correspond to points where closure has occurred. Closure in these calculations occurred in a similar manner to that observed in [24]. On unloading from the maximum load, the surfaces at the original location of the crack tip ($x_1 = 0$) first come into contact. Further reduction in the applied K_I results in this contact zone spreading from the original crack tip to the current location of the crack tip. Complete closure with contact of the crack faces at the current location of the crack tip occurs at an applied stress intensity factor $K_I = K_{cl}$. Upon reloading, the crack faces first separate at the current location of the crack when $K_I = K_{op}$. Continued loading results in the contact zone retracting towards the original location of the crack tip until finally the crack opens completely. In the simulations here $K_{cl} \approx K_{op}$. However, consistent with the intermittent nature of the cyclic crack advance in most of the calculations, K_{op} varies substantially from cycle to cycle in any given calculation. The average values of K_{op} over the number of cycles computed are shown in Fig. 6b: for $R = 0.1$ and 0.3 there is a general trend for K_{op}/K_{max} to decrease with increasing ΔK_I, which is consistent with experimental observations of crack closure in fatigue in aluminum by Ritchie et al. [4]. There is no clear trend for K_{op} for the calculations with $R = 0.5$. This may be because computations for $R = 0.5$ were performed only for relatively low values of applied ΔK_I as the large plastic zone sizes associated with $R = 0.5$ limited the calculations that could be carried out.

The effective stress intensity range ΔK_I^{eff} is defined as

$$\Delta K_I^{eff} = \begin{cases} K_{max} - K_{op} & \text{for } K_{min} < K_{op} \\ \Delta K_I & \text{for } K_{min} \geq K_{op} \end{cases} \tag{9}$$

Using this prescription, the da/dN versus ΔK_I data are replotted in Fig. 6a as da/dN versus ΔK_I^{eff}. To within numerical scatter, all the data collapses onto a single master curve with no dependence on R.

This indicates that the R dependence of the crack growth rate is a crack closure effect and that the crack growth rate is governed by the effective value of ΔK_I over the range investigated here.

Crack closure as modeled through the irreversible cohesive relation has a profound effect on the crack growth behavior. The extent of crack closure is governed by Δ_s which represents the asymptotic value of the oxide layer thickness formed on the newly created surface. The effect of Δ_s on the crack growth behavior is shown in Fig. 7, where crack advance versus time curves are plotted for $\Delta_s = 4\delta_n$, $8\delta_n$ and $\Delta_s \rightarrow \infty$ for a loading characterized by $R = 0.1$ and $\Delta K_I / K_0 = 1.062$. With $\Delta_s \rightarrow \infty$ the oxide layer thickness is continuously increasing with crack opening displacement. This results in da/dN increasing with the number of cycles and a "steady" da/dN is not achieved. Decreasing Δ_s reduces the irreversibility in the cohesive relation with the cohesive relation becoming completely reversible for $\Delta_s = 0$. Thus, reducing Δ_s has the effect of decreasing the cyclic crack growth rates. From Fig. 7 we see that the crack advance versus time curves are not very sensitive to the choice of Δ_s in the range $4\delta_n$ to $8\delta_n$ with a "steady" da/dN being achieved in both cases. This range of Δ_s is in line with the oxide layer thicknesses of 2–6 nm reported for aluminum under ambient conditions [31]. Decreasing Δ_s below $4\delta_n$
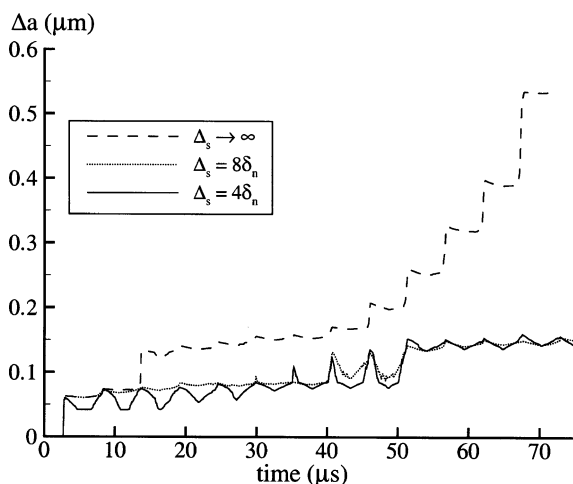
results in very low crack growth rates similar to those encountered with a fully reversible cohesive law while increasing Δ_s above $8\delta_n$ gives accelerating crack growth.

3.2. Fatigue in a single crystal

The single crystal analyzed is characterized by the same slip plane geometry and nucleation source and obstacle distribution as used to characterize the metal in the metal–ceramic interface problem, thus representing the fatigue behavior of that material. Symmetry about the crack plane is prescribed. Since qualitative features of the mode I crack growth behavior in the homogeneous single crystal were found to be similar to those of the interface crack, namely intermittent crack growth at intermediate values of ΔK_I and more steady cycle-by-cycle crack growth at threshold and high values of ΔK_I, only results for the da/dN versus ΔK_I behavior are presented.

The da/dN versus ΔK_I data for $R = 0.3$ is plotted in Fig. 8a. As in Fig. 6a, the da/dN values plotted are averages over the number of cycles computed. This was generally 20 and 10 for low and high values of ΔK_I, respectively. Again, there are two distinct regimes of behavior: a steeply rising $\log$(da/dN) versus $\log(\Delta K_I / K_0)$ curve in the threshold regime followed by a more gradual slope in the Paris regime. The Paris law exponent m in this case is ≈ 4.4 ($m = 2$ to 4 is typical for ductile metals, e.g. [4]). The crack closure stress intensity factor is plotted in Fig. 8b as a function of the applied ΔK_I. As in the interface crack calculations, K_{op} is taken as the average value over the number of cycles computed for each loading. The values of K_{op}/K_{max} decrease with ΔK_I in line with the experimental findings of Ritchie et al. [4]. The cyclic crack growth rate da/dN is also plotted in Fig. 8a as a function of ΔK_I^{eff}, with ΔK_I^{eff} calculated using Eq. (9). The effect of crack closure is more pronounced at the lower values of ΔK_I so that ΔK_{th}^{eff} is much less than ΔK_{th} and the cohesive relation may be overpredicting closure in the near-threshold regime. Crack closure also results in an exponent $m \approx 2.8$ for the modified Paris relation

$$\frac{\mathrm{d}a}{\mathrm{d}N} \propto (\Delta K_I^{eff})^m. \tag{10}$$

Fig. 7. Time evolution of the interface crack growth ($R = 0.1$, $\Delta K_I / K_0 = 1.062$) for three values of Δ_s.
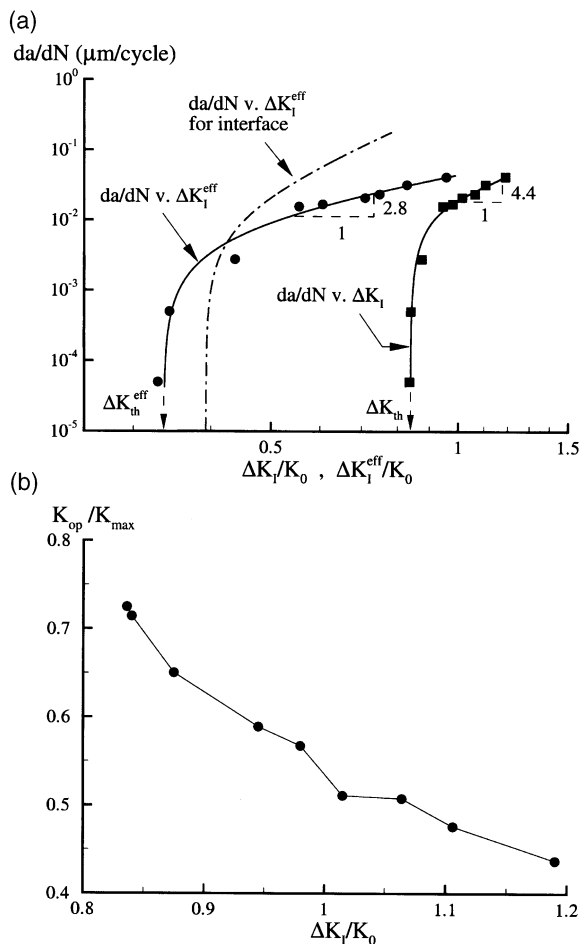
(a)

da/dN (μm/cycle)

(b)

K_{op}/K_{max}

Fig. 8. The cyclic crack growth rate da/dN versus $\Delta K_I/K_0$ and $\Delta K^{eff}_I/K_0$ for the mode I cyclic loading of the single crystal ($R = 0.3$). The slopes of the curves marked correspond to the Paris law exponents for the curves fitted through the numerical results. (b) The normalized crack opening stress intensity factor K_{op}/K_{max} versus $\Delta K_I/K_0$ for $R = 0.3$.

For comparison purposes the "best-fit" da/dN versus $\Delta K^{eff}_I/K_0$ curve for the interface crack from Fig. 6a is replotted in Fig. 8a. The effect of the mode mixity at the interface is to increase the fatigue threshold of the interface crack but to reduce its resistance to cyclic crack growth at higher values of applied ΔK_I. These conclusions are expected to be strongly dependent on the degree of mode mixity and hence affected by the

cohesive properties and the boundary conditions applied.

Rather uniformly spaced slip traces at $\theta = 60°$ in the wake of the propagating fatigue crack are also seen for the single crystal. Fig. 9 shows contours of Γ at the twelfth load peak for the case with $R = 0.3$ and $\Delta K_I / K_0 = 1.19$. These slip traces closely resemble those for the interface crack in Fig. 4. Moreover, this deformation field is similar to that in the experiments of Laird and Smith [8] and Neumann [19] for cyclic crack growth in metals. Note the high values of Γ parallel to the crack resulting from dislocation activity on the $\theta = 0°$ slip planes (Fig. 9).

4. Discussion

In the calculations here and in [24,35], the fracture behavior is an outcome of the interplay between the cohesive and plastic flow properties. Under monotonic loading conditions, with a sufficiently low density of dislocation sources, only isolated dislocations are generated and crack propagation takes place in a brittle manner. When ample nucleation sources are available and the
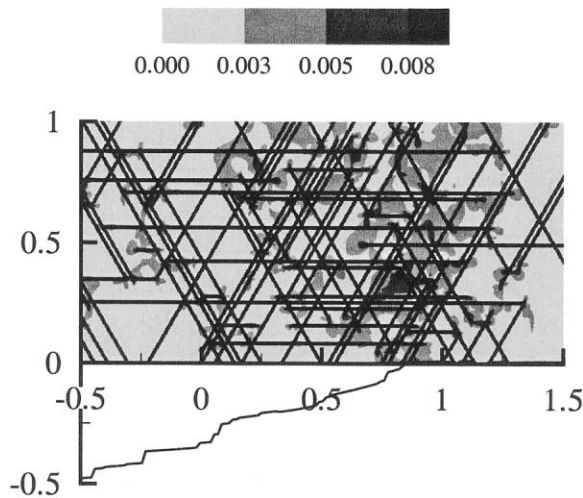

Fig. 9. Contours of the total slip $\Gamma = \sum |\gamma^{(\alpha)}|$ at the 12th load peak for a loading characterized by $R = 0.3$ and $\Delta K_I / K_0 = 1.19$ in the case of the single crystal. All distances are in μm. The crack opening profile (displacements magnified by a factor of 20) is plotted below the x_1-axis.

obstacle density is sufficiently low, the dislocations strongly relax the near-tip stresses, resulting in continued crack tip blunting without crack propagation. In these circumstances, ductile fracture would eventually take place by a process of void nucleation, growth and coalescence. The circumstances considered in this paper fall in an intermediate regime where, under monotonic loading, decohesion occurs in the presence of plastic deformation because of the high local stress concentrations ahead of the crack that arise from the near-tip dislocation structures. Under cyclic loading conditions, the increasing dislocation density near the crack tip, with the associated increase in stress level, is what allows the decohesion mechanism to operate at lower imposed driving forces than are needed under monotonic loading conditions.

Based on the experimental work of Laird and Smith [8] and Neumann [19], fatigue crack growth in ductile metals is often presumed to occur by an alternating slip mechanism which is a deformation-controlled phenomenon that does not require high stresses. By contrast, in our framework fracture is both a deformation- and a stress-governed phenomenon and takes place by a mechanism that is possible under both monotonic and cyclic loading conditions. Crack propagation under monotonic loading occurs in "spurts" with slip traces on the $\theta = 60°$ slip planes being left behind at rather uniform intervals in the wake of the propagating crack. This is consistent with the experimental observations of Kysar [39] for small amounts of monotonic crack growth along a copper–sapphire interface. In our calculations, more or less uniformly spaced slip traces occur on the $\theta = 60°$ slip planes under monotonic loading and in the wake of a propagating fatigue crack, and the slip band spacings are about the same in the monotonic and cyclic loading calculations. The present calculations suggest that striations are not generally observed under monotonic loading because observations are usually made after fracture when more diffuse plastic deformation has occurred and smeared out the slip bands.

Experimentally there is a wealth of evidence relating to fatigue striations: these striations are ripples seen on the fatigue fracture surface of most ductile metals. In our calculations, we obtain fairly

uniformly spaced slip bands at $\theta = 60°$ which are very similar to the slip traces seen on metal surfaces in the wake of a propagating fatigue crack. These slip bands leave slip steps on the crack surface, giving rise to a staircase-like fracture surface (the crack profiles in Figs. 4 and 9). The striations that emerge in our calculations most closely resemble type B striations according to the classification scheme of Forsyth [40]. Indeed, experimental observations of Nix and Flower [41] show that type B striations result from atomic separation followed by crack tip blunting and dislocation nucleation with the slip band spacing corresponding to that of the surface striations. The mechanism of striation formation in our calculations is in remarkable accord with these observations.

Other types of striations (type A according to the Forsyth [40] classification scheme) are usually associated with off-plane crack growth. While it is possible in principle to allow off-plane crack growth in the cohesive surface framework, that is not accounted for in the calculations here. Other limitations that affect the prediction of striations include: (i) the calculations were carried out for at most 36 cycles while experimental observations are usually made after at least a few hundred cycles; and (ii) in our small-strain formulation stress concentrations due to surface steps are not accounted for, which may affect the evolution of the surface profile. Nevertheless, the present calculations provide a possible rational for the minimum striation spacing of ≈ 0.1–0.15 µm seen for a wide variety of materials [42]; namely that the minimum striation spacing is set by the interaction of the stress fields of the dislocations comprising the slip bands.

In our previous study on near-threshold fatigue behavior [24] we presented cyclic crack growth calculations with a reversible cohesive relation as may occur in vacuum. Crack growth in those calculations was solely due to the inherent irreversibility of dislocation motion. Striations are typically not seen for fatigue loading under high vacuum conditions, e.g. [43]. Fatigue calculations with a reversible cohesive relation were not carried out here as the high ΔK_I values (with correspondingly high dislocations densities) required to get sufficient crack growth made such computations pro-

hibitively time-consuming. It is worth noting, however, that crack closure did not occur in the near-threshold calculations in [24] when a reversible cohesive relation was used and that Nix and Flower [41] suggest that striations are closure induced.

The form of the $\log(\mathrm{d}a/\mathrm{d}N)$ versus $\log(\Delta K_\mathrm{I})$ curve seen experimentally, with a threshold and a Paris law regime, is captured in our analysis. In the near-threshold regime the $\log(\mathrm{d}a/\mathrm{d}N)$ versus $\log(\Delta K_\mathrm{I})$ curve is steeply increasing as a significant proportion of the driving energy is going into the work of separation with only small amounts of plastic dissipation in the bulk material. With increasing ΔK_I the plastic zone size increases resulting in increased plastic dissipation. This gives rise to the knee in the $\log(\mathrm{d}a/\mathrm{d}N)$ versus $\log(\Delta K_\mathrm{I})$ curve with the Paris law exponent m decreasing as the ratio of the plastic dissipation to the work of separation increases. This suggests that when the plastic dissipation is small compared to the work of separation, there is a high Paris law exponent and fatigue is essentially a cleavage process as in intermetallics, e.g. [44,45], and nickel-based superalloys [6]. On the other hand, in ductile metals the plastic dissipation is typically very large compared to the work of separation which would tend to reduce the Paris law exponent. Our model is capable of capturing the wide range of Paris law exponents seen experimentally through the interaction between the independently specified cohesive and material properties. It is expected that the Paris exponent m will approach 2 in the limit that plastic dissipation completely dominates, since in that limit the only relevant length scales, the size of the cyclic plastic zone and the crack opening displacement, scale as $(\Delta K_\mathrm{I})^2$.

The calculations presented here were carried out for relatively low values of ΔK_I and hence may pertain to a regime approaching Paris law behavior. In Fig. 6a the $\log(\mathrm{d}a/\mathrm{d}N)$ versus $\log(\Delta K_\mathrm{I})$ curves tend to converge but there is still an R dependence for the crack growth rates over the entire range of ΔK_I investigated here. The R dependence of the crack growth rates in our calculations is a crack closure effect with all the data for the interface crack collapsing onto a single curve when the Paris law is expressed in terms of $\Delta K_\mathrm{I}^\mathrm{eff}$ (Fig. 6a). The crack closure stress intensity factor $K_\mathrm{op}/K_\mathrm{max}$ as

modeled through our phenomenological irreversible cohesive relation decreases with increasing ΔK_I in line with the experimental findings of Ritchie et al. [4]. For a high applied ΔK_I, $\Delta K_\mathrm{I}^\mathrm{eff} = K_\mathrm{max} - K_\mathrm{op} \approx \Delta K_\mathrm{I}$ and thus we expect that the crack growth rate will have negligible R dependence in line with true Paris law behavior. It is worth emphasizing that while the calculations capture the observed closure behavior qualitatively, the present analysis has several limitations in this regard. For example, our phenomenological cohesive relation is not based on a quantitative consideration of oxidation kinetics and the small-strain formulation neglects changes in the surface geometry due to slip steps which can give rise to roughness-induced crack closure. These limitations can be addressed through ab initio calculations such as those recently undertaken by Jarvis et al. [46], which could provide the basis for a more accurate cohesive relation, and through a finite strain discrete dislocation formulation which accounts for geometry changes.

An indication of how the discrete dislocation predictions compare with what is observed experimentally is shown in Fig. 10 where numerically computed and experimental curves of $\mathrm{d}a/\mathrm{d}N$ and
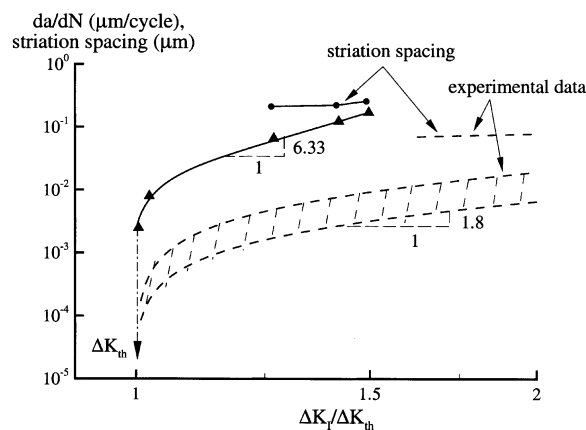

Fig. 10. A comparison between the predicted cyclic crack growth rate and experimental measurements of McNaney et al. [20] for the mode I cyclic loading of the interface crack ($R = 0.1$). The experimental values of ΔK_I from McNaney et al. [20] and the calculated values of ΔK_I are each normalized by the corresponding threshold value, ΔK_th. Also shown in the figure is a comparison between the predicted and measured striation spacings.

striation spacing versus ΔK_I are shown. The experimental data are taken from McNaney et al. [20] and, to provide a basis for the comparison between the numerical and the experimental data, each value is normalized by its threshold value, ΔK_{th}. The experimental measurements in [20] were carried out using four-point bend Al_2O_3–Al–Al_2O_3 sandwich specimens for a load ratio of $R = 0.1$ and for an applied ΔK_I ranging from approximately 1 to 10 MPa $\sqrt{m}$ (only the portion of the data corresponding to the computed range is shown in Fig. 10). The sandwiched metal layer was made from high-purity (99.999%) polycrystalline Al and its thickness varied between 100 and 500 µm. McNaney et al. [20] found that the fatigue crack growth rates along the Al–Al_2O_3 interfaces were reasonably independent of the Al layer thickness. The numerical simulations, in contrast, are for Al single crystals bonded to a rigid substrate in small-scale yielding. Thus, the comparison is of dissimilar situations, but we have not found da/dN versus ΔK_I data for fatigue crack growth along a single-crystal metal–ceramic interface. The predicted Paris law exponent of about 6 is greater than the measured exponent of ≈ 1.8. Factors contributing to the more brittle fatigue crack growth in the calculations include: (i) the bonding in the McNaney et al. [20] experiments may be stronger than that modeled here; (ii) the material parameters used in the calculations, i.e. the strength and density of the dislocation sources and obstacles, may not be representative of the particular alloy in the experiments in [20]; (iii) a high loading rate is used in the calculations to reduce the computing time and this acts to decrease the amount of plastic dissipation; (iv) grain boundary interactions which retard crack growth and increase plastic dissipation occur in the experiments but not in the single-crystal calculations; (v) crack tip blunting effects are not taken into account in our small-strain analyses; and (vi) crack closure which plays a significant role for $R = 0.1$ may not be modeled accurately as discussed above. A comparison between the predicted striation spacings and the measurements of McNaney et al. [20] is also shown in Fig. 10. Consistent with the experimental findings, the numerical calculations predict striation spacings that exceed the crack growth increment per cycle and

show less dependence on ΔK_I than the crack growth rate. However, the predicted striation spacings are greater than the experimental measurements which may be due to the reduced plasticity and more brittle nature of fatigue in the calculations.

5. Concluding remarks

We have carried out analyses of fatigue crack growth along metal–ceramic interfaces and in single crystals under remote mode I plane strain conditions. Plastic flow arises from the collective motion of large numbers of discrete dislocations and the fracture properties are embedded in a cohesive surface constitutive relation. The only difference between the boundary problem formulations for monotonic and cyclic loading is the prescribed time variation of the remote stress intensity factor.

- Crack growth occurs under cyclic loading conditions when the driving force is smaller than that needed for the crack to grow under monotonic loading conditions.
- Two distinct regimes of behavior emerge naturally from the calculations: a steeply rising $\log(da/dN)$ versus $\log(\Delta K_I)$ curve in the threshold regime followed by a more gradual slope in the Paris regime. This change in slope is due to the increased plastic dissipation at the higher ΔK_I values.
- Steady cycle-by-cycle crack growth occurs for near-threshold and high values of applied ΔK_I while crack growth is more intermittent at intermediate values of the applied ΔK_I.
- Striations emerge as traces of concentrated slip on the newly created free metal surface for cracks propagating along metal–ceramic interfaces as well as for cracks in single crystals.
- The striation spacing is of the order of the amount of crack growth per cycle in the Paris law regime and greater than the amount of crack growth per cycle in the near-threshold regime.
- The calculations here and in [24] rationalize a wide range of observed fatigue crack growth behavior within a unified framework.

Acknowledgements

References

[1] Paris PC, Gomez MP, Anderson WP. Trend Eng 1961;13:9.
[2] Davidson DL, Lankford J. Int Mater Rev 1992;37:45.
[3] Suresh S. Fatigue of materials. Cambridge (UK): Cambridge University Press, 1998.
[4] Ritchie RO, Yu W, Blom AF, Holm DK. Fatig Fract Eng Mater Struct 1987;10:343.
[5] Chan KS, Hack JE, Leverant GR. Metall Trans 1987;18A:581.
[6] Mercer C, Soboyejo ABO, Soboyejo WO. Acta Mater 1999;47:2727.
[7] Frost NE. In: Yokobori T, Kawasaki T, Swedlow JL (eds). Proceedings of the First International Conference on Fracture, Sendai (Japan), 1965, vol. 2, pp. 723–35.
[8] Laird C, Smith GC. Philos Mag 1962;7:847.
[9] McClintock FA. In: Liebowitz H, editor. Fracture 1971;3:47.
[10] McClintock FA. In: Drucker DC, Gilman JJ, editors. Fracture of solids 1963;20:65.
[11] Weertman J. Int J Fract 1966;2:460.
[12] Rice JR. Fatigue crack propagation, ASTM STP 1967;415:247.
[13] Nguyen O, Repetto A, Ortiz M, Radovitzky RA. Int J Fract 2001;110:351.
[14] Riemelmoser FO, Gumbsch P, Pippan R. Mater Trans 2001;42:2.
[15] Pippan R. Acta Metall Mater 1991;39:255.
[16] Riemelmoser FO, Pippan R. Mater Sci Eng A 1997;234-236:135.
[17] Riemelmoser FO, Pippan R, Stüwe HP. Int J Fract 1997;85:157.
[18] Wilkinson AJ, Roberts SG, Hirsch PB. Acta Mater 1998;46:379.
[19] Neumann P. Acta Metall 1969;17:1219.
[20] McNaney JM, Cannon RM, Ritchie RO. Acta Mater 1996;44:4713.
[21] Gaudette F, Suresh S, Evans AG. Metall Mater Trans 1999;30A:763.
[22] Peralta P, Ramamurty U, Suresh S, Campbell GH, King WE, Mitchell TE. Philos Mag 2000;A80:2109.
[23] Cleveringa HHM, Van der Giessen E, Needleman A. Int J Plast 1999;15:837.
[24] Deshpande VS, Needleman A, Van der Giessen E. Acta Mater 2001;49:3189.
[25] Morrissey JW, Rice JR. J Mech Phys Solids 1998;46:467.
[26] Cannon RM, Dalgleish BJ, Dauskardt RH, Oh TS, Ritchie RO. Acta Metall Mater 1991;39:2145.
[27] Kubin LP, Canova G, Condat M, Devincre B, Pontikis V, Bréchet Y. Solid State Phenomena 1992;23-24:455.
[28] Xu X-P, Needleman A. Modeling Simul Mater Sci Eng 1993;1:111.
[29] Gupta V, Yuan J. J Appl Phys 1993;74:2397.
[30] Rice JR. J Appl Mech 1968;35:379.
[31] Do T, Splinter SJ, Chen C, McIntyre NS. Surf Sci 1997;387:192.
[32] Rice JR. J Appl Mech 1988;55:98.
[33] Hutchinson JW, Suo Z. Adv Appl Mech 1991;29:63.
[34] Cleveringa HHM, Van der Giessen E, Needleman A. Mater Sci Eng A 2001;317:37.
[35] Cleveringa HHM, Van der Giessen E, Needleman A. J Mech Phys Solids 2000;48:1133.
[36] Van der Giessen E, Needleman A. Modeling Simul Mater Sci Eng 1995;3:689.
[37] Elber W. Eng Fract Mech 1970;2:37.
[38] Budiansky B, Hutchinson JW. J Appl Mech 1978;45:267.
[39] Kysar JW. Acta Mater 2000;48:3509.
[40] Forsyth PJE. Acta Metall 1963;11:703.
[41] Nix KJ, Flower HM. Acta Metall 1982;30:1549.
[42] Grinberg NM. Int J Fatig 1984;6:229.
[43] Pelloux RMN. Trans Am Soc Metall 1969;62:281.
[44] Harding TS, Wayne Jones J. Metall Mater Trans 2000;31A:1741.
[45] Dubey S, Soboyejo ABO, Soboyejo WO. Acta Mater 1997;45:2777.
[46] Jarvis EAA, Hayes RL, Carter EA. Chem Phys Chem 2001;1:55.